

## The High Resolution X-ray Spectrum of SS 433 using the *Chandra* HETGS

Herman L. Marshall, Claude R. Canizares, and Norbert S. Schulz

*Center for Space Research, MIT, Cambridge, MA 02139*

hermanm@space.mit.edu, crc@space.mit.edu, nss@space.mit.edu

### ABSTRACT

We present observations of SS 433 using the Chandra High Energy Transmission Grating Spectrometer. Many emission lines of highly ionized elements are detected with the relativistic blue and red Doppler shifts. The lines are measurably broadened to  $1700 \text{ km s}^{-1}$  (FWHM) and the widths do not depend significantly on the characteristic emission temperature, suggesting that the emission occurs in a freely expanding region of constant collimation with opening angle of  $1.23 \pm 0.06^\circ$ . The blue shifts of lines from low temperature gas are the same as those of high temperature gas within our uncertainties, again indicating that the hottest gas we observe to emit emission lines is already at terminal velocity. This velocity is  $0.2699 \pm 0.0007c$ , which is larger than the velocity inferred from optical emission lines by  $2920 \pm 440 \text{ km s}^{-1}$ . Fits to the emission line fluxes give a range of temperatures in the jet from  $5 \times 10^6$  to  $1 \times 10^8 \text{ K}$ . We derive the emission measure as a function of temperature for a four component model that fits the line flux data. Using the density sensitive Si XIII triplet, the characteristic electron density is  $10^{14} \text{ cm}^{-3}$  where the gas temperature is about  $1.3 \times 10^7 \text{ K}$ . Based on an adiabatic expansion model of the jet and a distance of 4.85 kpc, the electron densities drop from  $\sim 2 \times 10^{15}$  to  $4 \times 10^{13} \text{ cm}^{-3}$  at distances of  $2 - 20 \times 10^{10} \text{ cm}$  from the apex of the cone that bounds the flow. The radius of the base of the visible jet is estimated to be  $\sim 10^8 \text{ cm}$  and the mass outflow rate is  $1.5 \times 10^{-7} M_\odot \text{ yr}^{-1}$ . The kinetic power is  $3.2 \times 10^{38} \text{ erg s}^{-1}$ , which is  $\times 1000$  larger than the unabsorbed 2-10 keV X-ray luminosity. The bremsstrahlung emission associated with the lines can account for the entire continuum; we see no direct evidence for an accretion disk. The image from zeroth order shows extended emission at a scale of  $\sim 2''$ , aligned in the general direction of the radio jets.

*Subject headings:* X-ray sources, individual: SS 433

## 1. Introduction

The Galactic X-ray binary SS 433 is the only known astrophysical system where relativistically red- and blue-shifted lines are observed from high  $Z$  elements. Lines from the H Balmer series were detected by Margon et al. (1977) and modelled kinematically by Abell & Margon (1979), Fabian & Rees (1979), and Milgrom (1979) as emission from opposing jets emerging from the vicinity of a compact object that precesses about an axis inclined to the line of sight. The precise description of the line positions was given by Margon & Anderson (1989): the jet velocity,  $v_j$ , is  $0.260c$  and its orientation precesses with a 162.5 day period in a cone with half-angle  $19.85^\circ$  about an axis which is  $78.83^\circ$  to the line of sight. The lines from the jet are Doppler shifted with this period so that the maximum redshift is about 0.15 and the maximum blueshift is about -0.08. The X-ray source undergoes eclipses at a 13.0820 day period. Assuming uniform outflow, the widths of the optical lines were used to estimate the opening angle of the jet:  $5^\circ$  (Begelman et al. 1980). For more details of the optical spectroscopy, see the review by Margon (1984).

SS 433 has radio jets oriented at a position angle of  $100^\circ$  (east of north) which show an oscillatory pattern that can be explained by helical motion of material flowing along ballistic trajectories (Hjellming & Johnston 1981). Using VLBI observations of ejected knots, Vermeulen et al. (1993) independently confirmed the velocity of the jet and the kinematic model and also derived an accurate distance:  $4.85 \pm 0.2$  kpc, which we adopt throughout our analysis. The radio jets extend from the milliarcsec scale to several arcseconds, a physical range of  $10^{15-17}$  cm from the core. The optical emission lines, however, originate in a smaller region,  $< 3 \times 10^{15}$  cm across, based on light travel time arguments (Davidson & McCray 1980). At the same position angle is large scale X-ray emission that extends  $\pm 30-35'$  to about  $1.5 \times 10^{20}$  cm (Watson et al. 1983).

Marshall et al. (1979) were the first to demonstrate that SS 433 is an X-ray source. Their *HEAO-A* spectrum could be modelled as thermal bremsstrahlung with  $kT = 14.3$  keV and emission due to Fe-K was detected near 7 keV. They also found that the X-ray luminosity,  $\sim 10^{36}$  erg s $^{-1}$ , was much lower than the inferred power in kinetic energy:  $\sim 10^{40}$  erg s $^{-1}$ . *EXOSAT* X-ray observations showing that the 6.7 keV line appeared to shift with the precession phase were interpreted as detecting Fe XXV from 10 keV gas (Watson et al. 1986). Using *Ginga*, Brinkmann et al. (1991) concluded that  $kT$  should be 30 keV while Kotani et al. (1996) obtained a value of 20 keV based on the ratio of Fe XXV and Fe XXVI line fluxes from *ASCA* observations. Brinkmann et al. (1991) and Kotani et al. (1996) developed the model that the X-ray emission originates near the base of the jets which are adiabatically expanding and cooling until  $kT$  drops to about 100 eV at which point the jet is thermally unstable. Kotani et al. (1996) found that the redshifted Fe XXV line was fainter

relative to the blueshifted line, than expected from Doppler intensity conservation, leading them to conclude that the redward jet must be obscured by neutral material in an accretion disk. Although the *ASCA* spectra showed emission lines that were previously unobserved, the lines were not resolved spectrally and lines below 2 keV were difficult to identify.

SS 433 was observed using the High Energy Transmission Grating Spectrometer (HETGS) in order to resolve the X-ray lines, detect fainter lines than previously observed and measure lower energy lines that could not be readily detected in the *ASCA* observations. A description of the HETGS and its performance are given by Canizares et al. (2001). An important feature of the HETGS is that spectra are obtained independently and simultaneously using the High Energy Gratings (HEGs) and the Medium Energy Gratings (MEGs). The HEGs have  $\times 2$  higher spectral resolution and greater effective area above 4 keV than the MEGs while the MEGs have an extended bandpass and more effective area for detecting low energy emission lines.

## 2. Observations and Data Reduction

SS 433 was observed with the HETGS on 23 September 2000 (JD - 2451000. = 445.0 - 445.4). The precession phase was 0.51, based on the ephemeris determined by Margon & Anderson (1989) and the orbital phase was 0.67 using the orbital ephemeris of Gladyshev et al. (1987). The telescope roll angle was set so that the dispersion direction was nearly perpendicular to the jet axis. The exposure time was 28676 s, determined by  $t_{exp} = N(t_{frame} - t_{shift})$ , where  $N$  is the number of frames with detected events,  $t_{frame}$  is the ACIS-S frame time (3.241 s) and  $t_{shift}$  is the frame shift time (0.041 s). This computation corrects for the “readout streak” exposure because the streak data are not included in the analysis.

### 2.1. Imaging

Based on the HETGS spectral fits (see sec. 2.2), we expected to observe about 1.4 count/s in zeroth order. The average count rate in zeroth order was measured to be about 0.15 count/s, so we conclude that the image is heavily affected by pileup, given the 3.2 s frame times. Briefly, pileup occurs when two or more events are detected within an event region ( $3 \times 3$  pixels) in a readout or frame time. Pileup has three important effects: 1) event energies are combined so that it is impossible to determine the energies of the original events, 2) the event grade (denoting the distribution of charge among the 9 pixels) changes and can often end up as a grade that is normally eliminated in processing, reducing the apparent

count rate, and 3) having a highly nonlinear dependence on the local count rate, the cores of point sources are more affected than the wings so the appearance can be distorted. Spectral analysis of heavily piled zeroth order data can be challenging and was deemed to be of limited value compared to the HETGS spectra.

The zeroth order image, shown in Fig. 1, is distinctly elongated in the E-W direction. Due to event pileup, we cannot determine if the image matches that of a point source within  $1''$  of the core. Profiles along the E-W and N-S directions should be affected by pileup in the same way, however we find that they are clearly different, as shown in Fig. 2: there are “shoulders” to the E-W profile that do not appear in the N-S profile. Again, these profiles are difficult to compare to point source models due to the nonlinear effects of pileup, so these one-dimensional profiles are most useful only for comparing to each other.

We associate the excess emission in the E-W direction with the arcsec-scale radio jet, as observed by Hjellming & Johnston (1981) using the VLA. A radial profile of the extended emission was computed by determining the counts in two E-W azimuthal sectors and subtracting normalized profiles using the remaining N-S azimuths. The profile is shown in Fig. 3. This method nulls the point source, so the  $1''$  bin centered on the source shows no significant excess flux. Extended flux is detected 1-2'' from the core and drops rapidly with distance from the image centroid until it is undetectable beyond  $6''$ . We estimate that the total count rate from the extended jets is about  $0.008 \pm 0.0005$  count/s, accounting for about 0.6% of the flux within  $5''$  of the source centroid.

A set of cross dispersion profiles were derived for continuum regions and for several line regions of the dispersed spectrum. For comparison, profiles for the same wavelength regions were determined from a point-like calibration source, PKS 2155–304 (observation ID 1705). The profiles are indistinguishable from each other and are consistent with that of the point source. Thus, we conclude that the most of the emission lines and the continuum originate from the same region on a scale of  $< 1''$ . The extended, elongated emission detected in the zeroth order image would not be discernable in the cross dispersion profiles at the same low fractional power due to the slight astigmatism of the grating optics in the cross dispersion direction.

## 2.2. Spectra

The spectral data were reduced starting from level 1 data provided by the Chandra X-ray Center (CXC) using IDL custom processing scripts; the method is quite similar to standard processing using standard CXC software but was developed independently for HETGS cal-

ibration work. The procedure was to: 1) restrict the event list to the nominal grade set (0,2,3,4, and 6), 2) remove the event streaks in the S4 chip (which are not related to the readout streak), 3) estimate exposure including accounting for frame shift time, 4) determine the location of zeroth order using Gaussian fits to one dimensional profiles, 5) rotate events from sky coordinates to compensate for the telescope roll, 6) compute the dispersed grating coordinates ( $m\lambda$  and  $\phi$ ) using the grating dispersion angles and the dispersion relation, 7) correct event energies for detector node-to-node gain variations, 8) select  $\pm 1$  order events using  $|E_{ACIS} * m\lambda/(hc)| - 1 < \Delta$  where  $E_{ACIS}$  is the event energy inferred from the ACIS pulse height, and  $\Delta$  is 0.20 for the MEG and 0.15 for the HEG events, 9) eliminate events in bad columns where the counts in an histogram deviated by  $5\sigma$  from a 50 pixel running median, 10) select “source” events spatially within a rectangular region  $3.6''$  of the center of the dispersion line and background events in the bands  $7.2$  to  $21.6''$  from the dispersion line, 11) bin MEG (HEG) events at  $0.01\text{\AA}$  ( $0.005\text{\AA}$ ), 12) eliminate data affected by detector gaps, and 13) generate and apply an instrument effective area based on the pre-flight calibration data.

The spectra are shown in Figs. 4 to 7. Figure 4 shows the flux corrected spectrum, combining the MEG and HEG data with statistical weighting. There are many broad emission lines and a significant continuum. At the low energy end, the lines are so broad that it becomes difficult to discern them from the continuum. A simple power law fit to the continuum gave a very good fit to the 0.8-8 keV spectral data:  $n(E) = AE^{-\Gamma}e^{-N_H\sigma(E)}$ , where  $n(E)$  is the photon flux in  $\text{ph cm}^{-2} \text{s}^{-1} \text{keV}^{-1}$ ,  $E$  is energy in keV,  $N_H$  is the line of sight neutral hydrogen density due to the interstellar medium (ISM) primarily,  $\sigma(E)$  is the opacity of the ISM with cosmic abundances, and the best fit parameters are  $A = 0.015 \text{ ph cm}^{-2} \text{ s}^{-1} \text{ keV}^{-1}$ ,  $\Gamma = 1.35$ , and  $N_H = 9.5 \times 10^{21} \text{ cm}^{-2}$ . The HEG and MEG spectra give comparable results. The  $N_H$  and  $\Gamma$  are about 30% higher but  $A$  is 30% lower than that found by Kotani et al. (1996) although the observations were obtained at the same precession phase. The average 2-10 keV luminosity is about  $3.1 \times 10^{35} \text{ erg s}^{-1}$  and was observed to decrease about 10% during the observation.

Line fluxes are given in table 1. Lines were fit to the MEG and HEG data jointly in six wavelength ranges after subtracting a polynomial fit to the continuum. To allow for slight deviations from the continuum model, a constant level was allowed to vary in each interval. The line positions and fluxes were allowed to vary from initial estimates for each line but the Gaussian widths were fitted to a single value in each range. The widths are given in table 2. Uncertainties were estimated upon fixing the parameters of all other lines in a given interval to their best fit values. Only statistical errors are quoted; systematic uncertainties other than possible line misidentifications are expected to be smaller than 10%.

A redshift was measured for each line or line triplet after determining the ID based on the expected shifts of the blue and red jets from the kinematic model. For the precession phase of our observation, the predicted blue- and red-shifts were -0.0670 and 0.1384, using the equation and parameters in table 1 of Margon & Anderson (1989). Wavelengths of line blends were obtained using wavelengths from APED<sup>1</sup> weighted by the relative fluxes of each component, which was especially important for the He-like triplets. The S XV and Si XIII triplets were treated somewhat differently. We determined more precise redshifts for these blends fitting the line profiles with several Gaussian components of variable widths but we fixed the rest wavelengths to the values given by APED, as implemented in ISIS<sup>2</sup>. Fig. 8 shows the results of jointly fitting the MEG and HEG data. The Si XIII line is used to estimate the density in the jet in section 4. In the red jet system, it was too difficult to measure an accurate redshift for the Si XIII triplet due to blending with Mg XII from the blue jet and to its low flux. The identified lines were then grouped according to redshift. Only one line was not assigned to either the red or blue jets: a neutral Fe-K line at rest in the observed frame. It is unresolved at HEG resolution, indicating a FWHM < 1000 km s<sup>-1</sup>.

### 3. Line Widths and Positions

Table 1 shows that the Doppler shifts of the lines in the blue jet system are consistent with a single velocity to within the uncertainties, as are those in the red jet system, although there are very few positively identified lines in the red jet. There are a few deviations that are not likely to be indicative of intrinsic variations. The lines generally responsible for the largest deviations are mostly weak, such as Ca XX, or are weak He-like triplets, such as Ar XVII and Mg XI. Furthermore, all deviations are substantially smaller than the observed line widths, which are of order 0.006 (FWHM). We determine that the Doppler shift of the blue jet was  $z_b = -0.0779 \pm 0.0001$  during this observation. For the red jet, the unblended lines detected at  $3\sigma$  or better give an estimated redshift of  $z_r = 0.1550$  with a formal uncertainty of 0.0004. There is marginal evidence that the Fe XXV line has a higher redshift than the other three lines. The difference is small,  $\sim 800$  km s<sup>-1</sup>, and could instead result from underestimated uncertainties because the two faintest lines are only marginally detected and the Fe XXIV line could even be misidentified. No other lines from the red jet show positive velocity deviations except Si XIII, which is severely blended with the Mg XII line from the blue jet. The spectral shifts are comparable to values obtained from a model

---

<sup>1</sup>See <http://hea-www.harvard.edu/APEC/aped/general.html> for more information about APED.

<sup>2</sup>See <http://space.mit.edu/CXC/ISIS> for more information about ISIS.

fitted to measurements of the H- $\alpha$  lines taken from the same precession cycle (Douglas Gies, private communication) within the large intrinsic variations.

Assuming perfectly opposed jets at an angle  $\alpha$  to the line of sight, the Doppler shifts of the blue and red jets are given by

$$z = \gamma(1 \pm \beta\mu) - 1 \quad (1)$$

where  $v_j = \beta c$  is the velocity of the jet flow,  $\gamma = (1 - \beta^2)^{-1/2}$ , and  $\mu = \cos \alpha$ . The blue (red) Doppler shift is obtained by using the  $- (+)$  sign. With high accuracy redshifts, we can obtain an estimate of the  $\gamma$  and  $\beta$  by adding the redshifts to cancel the  $\beta\mu$  terms:

$$\gamma = \frac{z_b + z_r}{2} + 1 \quad (2)$$

giving  $\beta = 0.2699 \pm 0.0007$ . Comparing to the value derived by Margon & Anderson (1989) for the H- $\alpha$  lines, the velocities of the X-ray lines are larger by  $2920 \pm 440 \text{ km s}^{-1}$ . In order to reduce our estimate of  $\beta$  to within  $3\sigma$  of the value derived from the H- $\alpha$  lines, the more uncertain X-ray Doppler shift – the redshift – would have to be as small as 0.1520. A redshift this small would place the centroid of the best measured line, Fe XXV, practically outside the observed line, so we have some confidence in the jet velocity measurement. Substituting our value for  $\beta$  back into Eq. 1 and solving for  $\alpha$  gives the angle of the jet to the line of sight during our observation:  $\alpha = 65.46^\circ \pm 0.07^\circ$ .

All jet lines are clearly resolved. The line widths in table 2 are consistent with the weighted average value ( $\sigma$ ) of  $729 \pm 34 \text{ km s}^{-1}$  or FWHM =  $1710 \pm 80 \text{ km s}^{-1}$ . There is only marginal evidence for a trend that the lower energy lines are slightly narrower than average. The widths of the red jet lines are consistent with that of the blue jet.

The line widths are too large to result from thermal broadening for  $kT < 10 \text{ keV}$  (see sec. 4) –  $100\text{-}200 \text{ km s}^{-1}$  – so we ascribe the widths to Doppler broadening that would result from the divergence of a conical outflow (Begelman et al. 1980). Fig. 9 shows the jet geometry, defining  $r$  as the distance along the cone from the apex and  $R = \Theta r$  is the jet cross sectional radius at  $r$ . We assume that the density is uniform through the cone’s cross section and that the component of the velocity that is parallel to the jet axis is the same for all fluid elements in the slice. Differentiating Eq. 1 with respect to  $\alpha$  gives the line width at zero intensity for material flowing within a small angle  $\Delta\alpha$  of the jet axis:  $\Delta z = \gamma\beta \sin \alpha \Delta\alpha$ . Assigning  $\Delta\alpha = \Theta$  gives  $\Theta$  in terms of  $v_m = c\Delta z$ , the maximum velocity relative to line center:

$$\Theta = \frac{v_m}{\gamma\beta c \sin \alpha}. \quad (3)$$

The line profile can be determined using the geometry of a slice through the jet, shown in Fig. 10. The angle  $\theta$  is the flow direction of a jet fluid element relative to the jet axis on a chord at distance  $\rho = \theta r = \theta R/\Theta$  from the jet axis perpendicular to the direction to the observer. The strength of the emission line at this velocity relative to line center is proportional to the length of the chord:  $l = 2(R^2 - \rho^2)^{1/2} = 2R(1 - (\theta/\Theta)^2)^{1/2}$ . The line profile (given as line-of-sight velocity profiles) is

$$I(v) = I_0(1 - (v/v_m)^2)^{1/2}, \quad (4)$$

The line profile is well approximated by a Gaussian by matching the full widths at half maximum:  $2.35\sigma = 3^{1/2}v_m$ , giving  $v_m = 989 \pm 47 \text{ km s}^{-1}$  and  $\Theta = 0.61^\circ \pm 0.03^\circ$ .

#### 4. Modelling the Jet Emission Line Fluxes

Radiative recombination features are practically nonexistent. Two weak features are consistent with radiative recombination continua (RRC) from Ne X and Ne IX (see Table 1) but we do not detect the RRC of other ions with prominent recombination lines: Mg XII, Si XIII, Si XIV, S XV, and S XVI. At high temperatures, the RRC could be significantly broadened, making them nearly indistinguishable from the continuum. At the temperatures we derive for the gas based on line ratios and detailed fits to line fluxes, S and Si RRC should be broadened by  $\sim 0.3\text{\AA}$ , so they should be detectable if photoionization was a significant process. Finally, the He-like triplets are dominated by the resonance lines, so we conclude that photoionization is negligible and that the plasma is collisionally ionized.

Spectral analysis was performed using ISIS using the APED atomic data base of line emissivities and ionization balance. The observed flux of an emission line from a region with electron density  $n_e$  and temperature  $T$  is given by

$$f_i = \frac{J_i(T) \int n_e^2 dV}{4\pi D^2} = \frac{J_i(T) EM(T)}{4\pi D^2} \quad (5)$$

where  $f_i$  is the observed flux of ion transition  $i$  in photons  $\text{cm}^{-2} \text{ s}^{-1}$ ,  $J_i(T)$  is the emissivity of a thin thermal plasma in transition  $i$  in photons  $\text{cm}^3 \text{ s}^{-1}$  and cosmic abundances,  $EM(T)$  is the emission measure of material with temperature  $T$ , and all quantities are measured

in the rest frame of the plasma. For the conical jet geometry shown in Fig. 9 where the temperature varies with distance  $r$ , we approximate equation 5 by a sum over a discrete set of independent sections defined by  $0.5r_j < r < 1.5r_j$ :

$$f_i = \frac{\Omega \sum_j J_i(T_j) n_j^2 r_j^3}{4\pi D^2} \quad (6)$$

where  $\Omega = \pi\Theta^2$  and  $j$  indicates the component of a multi-temperature model where the average electron density is  $n_j$  and the average electron temperature is  $T_j$ .

Using the ratios of the H-like to He-like line fluxes, we can estimate the temperature of the gas that produces most of each element’s emission, ignoring, for now, the contributions to other emission lines. Using emissivities from the APED data base, we find temperatures in the range from 1.2 to 7.6 keV, shown in table 3. Emission measures,  $EM_{1T}$ , are also derived, assuming cosmic abundances and that all emission from each ion originates in gas of a single temperature given by the line ratio. The results show that there is a broad range of temperatures in the outflow ranging from 1 to 10 keV ( $10^7$ – $10^8$  K) and that each element’s emission lines sample a different region in the jet. These temperature estimates are independent of the elemental abundances and are approximately independent of the line-of-sight column density because the wavelengths of the H-like and He-like lines are similar so that the ISM opacities are nearly the same. The emission measure can be overestimated due to the contributions from regions of the jet at other temperatures and requires an estimate of the line of sight  $N_H$ .

The blue Si XIII and S XV forbidden and intercombination lines are somewhat blended with the broadened resonance lines but are discernably weaker. The multi-Gaussian line fits were used to determine the density- and temperature-sensitive line ratios defined by Porquet & Dubau (2000):  $R(n_e) = f/i$  and  $G(T_e) = (i + f)/r$ , where  $r$ ,  $i$ , and  $f$  are the strengths of the resonance, intercombination, and forbidden lines, respectively. For Si XIII, we find  $R = 1.18 \pm 0.26$  and  $G = 0.92 \pm 0.13$  and for S XV, we obtain  $R = 11 \pm 24$  and  $G = 0.65 \pm 0.20$ . The S XV line does not give a good constraint on the density so we rely on the Si XIII fit results. Using curves from Porquet & Dubau (2000), the value of  $G$  indicates that  $T_e > 3 \times 10^6$  K, which is consistent with the estimate of  $1.9 \times 10^7$  K given in table 3. At a  $T = 10^7$  K, the value of  $R$  gives of  $n_e \sim 10^{14}$  cm $^{-3}$ . Using the estimate of the emission measure from table 3 and assuming  $N_H = 10^{22}$  cm $^{-2}$ , we now have an estimate of the emission volume for gas at a temperature of  $\sim 10^7$  K:  $2 \times 10^{30}$  cm $^3$ .

For a conical geometry with the opening angle derived from the line widths, then we obtain  $r \sim 2 \times 10^{11}$  cm. Note that  $r$  is the distance from the *apex* of a cone, which may be truncated at the accretion disk. The jet flow takes about 20 s to reach this distance at  $0.27c$ ,

which is much longer than the recombination time at the estimated density,  $\sim 10^{-3}$  s, so ionization balance can be achieved in the flow. There is X-ray emission out to  $5''$  from the core at a scale of  $3.6 \times 10^{17}$  cm but we have not yet detected emission lines at this distance.

A more refined estimate of the emission measure distribution can be obtained by fitting the line flux data to a multi-temperature emission model assuming solar abundances. We obtained a moderately good fit to the line flux data with a model with four components, as given in table 4 and shown in Fig. 11. The ISM absorption was fitted simultaneously, giving  $N_H = 2.20 \pm 0.07 \times 10^{22}$  cm $^{-2}$ , substantially larger than estimated from the simplistic power law fit. The ratios of the line fluxes to the values predicted from the four component model are shown in Fig. 12. There are indications that the spectrum is somewhat more complex than our model indicates: there may be additional lines at 8.65 Å and 9.15 Å that are not included in the model, the lines at 7.3 Å (Mg XI 1s3p-1s $^2$ ) and 9.8 Å (Fe XXIV) appear to be somewhat stronger in the model than in the data, and the line at 11.2Å (Ne X, Fe XXIII) is  $\times 2$  stronger than predicted by the model. Almost all of the other line fluxes are explained to within 50% and the strongest lines are modelled to within 10-20%. We consider this to be a satisfactory agreement, given the poor statistics in the long wavelength portion of the spectrum which makes it difficult to measure weak lines from gas in the jet which might be cooler than  $6 \times 10^6$  K.

The continuum expected from the four component model of the blue jet is comparable to the observed continuum, so the abundances of Fe, S, Si, Mg, and Ne were increased by 30% relative to H and He in order to allow for continuum from the red jet and so that the observed continuum is not exceeded in the 4-7Å region. The overall fit to the data is very good, as shown in Figs. 5 to 7. In the 8-12Å region, the model predicts a continuum that is systematically low by up to a factor of two. An additional continuum component is required. With such a large contribution from thermal bremsstrahlung, any nonthermal emission that might arise in an accretion disk must be fainter than  $\sim 10^{34}$  erg s $^{-1}$ .

Weighted by the emission measures from detailed fits to emission line fluxes, the Si XIII emission is dominated by gas at a temperature of  $\sim 1.3 \times 10^7$  K, which is close to the temperature of the second component given in table 4. At  $1.3 \times 10^7$  K, the observed value of  $R$  gives  $\log n_e = 14.0 \pm 0.2$ . Thus, we assign a density of  $10^{14}$  cm $^{-3}$  to the second emission measure component. This component's radius is estimated from Eq. 6 which gives  $r = 1.22 \times 10^{11}$  cm. Assuming an asymptotic form of the adiabatic cooling of an freely expanding jet,  $T \propto r^{-4/3}$  (e.g. Eq. 4 from the paper by Kotani et al.), then we can estimate the radius of each emission component and, using Eq. 6, the electron density at that radius. The results are given in table 4. For a uniform outflow at constant velocity,  $n \propto r^{-2}$ , so we expect

$$EM(T) \propto n^2 r^3 \propto r^{-1} \propto T^{3/4}. \quad (7)$$

This line is plotted in Fig. 11, normalized to provide a good fit for  $T < 5 \times 10^7$  K. The emission measure at the highest temperature deviates from the expected relation by a factor of 2 but the two remaining measurements agree very well.

The jet mass outflow rate,  $\dot{m}$ , is computed from

$$\dot{m} = \pi * (r\Theta)^2 v_j (1 + X) \mu n_e m_p, \quad (8)$$

where  $X$  is the ratio of the total ion density to  $n_e$  and is about 0.92 for completely ionized gas at cosmic abundances,  $\mu$  is the mean molecular weight for this gas and  $m_p$  is the mass of the proton. We find  $\dot{m} = 1.5 \times 10^{-7} M_\odot \text{ yr}^{-1}$ , derived primarily from the three low temperature components. With our measurement of the jet velocity, we have a value for the jet kinetic luminosity:  $3.2 \times 10^{38} \text{ erg s}^{-1}$ , which is  $\times 1000$  larger than the unabsorbed 2-10 keV X-ray luminosity.

For the red jet, a simple analysis of the H- and He-like line flux ratios for Fe and Si gives a two component model with  $EM(T)$  values significantly lower than estimated for the blue jet, even after correcting for ISM using the higher  $N_H$  estimate and accounting for Doppler flux diminution. The results, given in table 3, are rather uncertain due to the weak Fe XXVI line and the blended Si XIII lines. Tentatively, it appears that the emission measures are 20-25% of those found for the blue jet. Kotani et al. (1996) obtained a similar result from *ASCA* data, obtaining a fraction of about 35% for just the Fe XXV line ratio. Kotani et al. (1996) cited two effects that would reduce the Fe line flux from the red jet relative to the blue jet: occultation of the hot inner zones by an accretion disk and attenuation by additional cold gas along the line of sight to the more distant red jet. Although the statistics are poor, the Fe XXVI to Fe XXV ratios are consistent:  $0.30 \pm 0.17$  for the blue jet and  $0.17 \pm 0.11$  for the red jet, so we find that the red and blue jet temperatures are similar. A longer observation is needed to obtain a better detection of the red Fe XXVI line. As to the attenuation hypothesis, we obtain about the same ratio of emission measures for lines near  $2\text{\AA}$  as those near  $7.5\text{\AA}$ , which would be difficult to explain in a scenario involving absorption by neutral gas.

## 5. Discussion and Summary

The X-ray lines are emitted in an optically thin region where  $T$  drops from  $1.1 \times 10^8$  K to  $6 \times 10^6$  K,  $n_e$  drops from  $2 \times 10^{15}$  to  $4 \times 10^{13}$   $\text{cm}^{-3}$ , at a distances up to  $2 \times 10^{11}$  cm from the jet base. The X-ray continuum is dominated by the thermal bremsstrahlung from the jet so any nonthermal emission from the core must be  $< 10^{34}$   $\text{erg s}^{-1}$  unless the abundances in the jet are substantially non-solar. Weak extended X-ray emission is observed out to  $\sim 10^{17}$  cm but the gas is likely to be too cool to emit X-rays thermally.

Line profile measurements are consistent with the interpretation that the emission lines originate in conical jets with constant opening angle and constant flow speed. The lines are not double peaked, which would be expected if the gas were confined to the rim of the conical outflow, as might occur if the heavy elements were entrained from gas surrounding a leptonic jet. The lines are not skewed, as might be expected if material was accelerated through a narrow “nozzle”. From the consistency and narrowness of the line widths, we have a very accurate measurement of the jet opening angle:  $1.23 \pm 0.06^\circ$ . The optical lines give a somewhat larger value which may indicate that the optical emission results from interactions of the rapidly moving jet with ambient material much further along the jet, as suggested by Begelman et al. (1980). The jet velocity we measure is  $0.2699 \pm 0.0007c$ , which is larger than the velocity inferred from optical emission lines by  $2920 \pm 440$   $\text{km s}^{-1}$ , lending support to the hypothesis that the optical and X-ray line emission regions are physically distinct.

The blueshifted radiative recombination continua of Ne X and Ne IX indicate that there is a region of cooler photoionized plasma in the jet. The line widths give a temperature estimate of about  $< 10^5$  K, which would be found in the jet at  $> 4 \times 10^{13}$  cm from the compact object, assuming the adiabatic expansion model. Correcting for interstellar absorption, the ratio of the Ne IX to Ne X fluxes is  $2.1 \pm 0.6$ , giving an ionization parameter of  $\xi \equiv L_x/(n_e r^2) \approx 40$ . For the constant velocity jet,  $n_e r^2$  is constant at about  $1.7 \times 10^{36}$   $\text{cm}^{-1}$  which would require a photoionizing power of  $7 \times 10^{39}$   $\text{erg s}^{-1}$ , greatly exceeding both the observed X-ray luminosity and the kinetic power in the jet. Even if this luminosity were present but somehow unobserved, it would still be difficult to understand why there are no detectable Mg or Si RRC.

As pointed out by Kotani et al. (1996), the electron scattering optical depth across the base of the jet should not be significantly larger than one because otherwise the emission lines would be significantly broadened by Comptonization, which would broaden lines by  $\delta\lambda \simeq \lambda(kT/m_e c^2)^{1/2} = 0.26$   $\text{\AA}$  for the Si resonance lines at about 6  $\text{\AA}$ . This level of broadening is not observed in the S or Si resonance lines where it would dominate the velocity broadening or produce a broad pedestal. For the innermost component of the jet emission model, we can estimate the electron scattering optical depth,  $\tau_{es} = n_e \sigma_T \Theta r = 0.3$ , or marginally optically

thin. Since  $n_e \propto r^{-2}$ ,  $\tau \propto r^{-1}$  so the rest of the jet must be optically thin to electron scattering as well.

The optical depth in the resonance lines is be significantly larger, however, and might explain the drop in emission measure at the highest temperatures seen in figure. In the region that emits the Si XIII resonance line, for example, we find that the resonant optical depth at line center is  $\tau_0 \approx 8$ , while  $\tau_{es} \approx 0.08$ . This means that resonance scattering would increase the effective path length of a line photon, thereby increasing the probability that it is Compton scattered out of the line core. The effective optical depth to line escape is approximately  $\tau_{eff} \approx (\tau_0\tau_{es})^{1/2}$ , (see Felton & Rees (1972) and Felton, Rees & Adams (1972)). For Si XIII,  $\tau_{eff} \sim 0.8$ , so Compton scattering may be marginally important (although a proper radiative transfer calculation using the jet geometry and velocity structure is warranted). In the hottest region of table 4  $\tau_{eff} \approx 1.5$  for the strongest resonance lines of Fe XXV and Fe XXVI, both of which have  $\tau_0 \approx 8$ . Using instead the density for this temperature expected by the adiabatic relation (Fig. 11) would give  $\tau_{eff} \approx 2.5$  for these lines. Therefore, one explanation for why the emission measure appears to deviate from the expected adiabatic relation (Fig. 11) is that the emission lines from the highest density regions are Compton scattered from the core due to resonance trapping, and simply contribute to the continuum.

A reduced emission measure at high temperature might also be expected if the cone of the jet is truncated at  $r_0 = 2.0 \times 10^{10}$  cm, so that the emission measure is integrated over a smaller volume than assumed. In this truncation model,  $n_e$  increases by  $\times 2$  for the highest temperature component in table 4 to about  $4 \times 10^{15}$  cm<sup>-3</sup>. A revised emission measure model is also shown in Fig. 11 and agrees with the data. The radius of the base of the visible jet is  $\Theta r_0 = 2.3 \times 10^8$  cm.

We note the interesting agreement between the expansion velocity of the jet perpendicular to the jet axis,  $v_j \sin \Theta = 866 \pm 41$  km s<sup>-1</sup>, and the sound speed in the rest frame of the flowing gas,

$$c_s = \left[ \frac{5kT}{3\mu m_p(1+X)} \right]^{1/2}, \quad (9)$$

which is 1149 km s<sup>-1</sup> for our estimate of the jet base temperature,  $T = 1.1 \times 10^8$  K. We speculate that this agreement is physical: the jet expands at the sound speed of hydrogen and that the heavier elements are coupled to the protons at the base of the jet. The coupling process is unknown but could be related to the jet acceleration process as both must affect protons and ions of high Z elements equally.

We thank the referee for many insightful comments on the submitted manuscript, especially for pointing out the importance of resonant line opacity. This work has been supported in part under NASA contracts NAS8-38249 and SAO SV1-61010.

## REFERENCES

- Abell, G. O. & Margon, B. 1979, *Nature*, 279, 701
- Begelman, M. C., Sarazin, C. L., Hatchett, S. P., McKee, C. F., and Arons, J. 1980, *ApJ*, 238, 722
- Brinkmann, W., Kawai, N., Matsuoka, M., and Fink, H. H. 1991, *A&A*, 241, 112
- Canizares et al. 2001, in preparation
- Davidson & McCray, 1980, *ApJ*, 240, 1082
- Fabian, A. C. & Rees, M. J. 1979, *MNRAS*, 187, 13P
- Felton, J. E. & Rees, M. J. 1972, *A&A*, 17, 226
- Felton, J. E. Rees, M. J. & Adams, T. F. 1972, *A&A*, 21, 139
- Gladyshev, S. A., Goranskii, V. P., and Cherepashchuk, A. M. 1987, *Sov. Astron.*, 31, 541
- Hjellming, R. & Johnston, S. 1981, *ApJ*, 246, L141
- Kotani, T., Kawai, N., Matsuoka, M., and Brinkmann, W. 1996, *PASJ*, 48, 619
- Margon et al. 1977, *ApJ*, 246, L141
- Milgrom, M. 1979, *A&A*, 76, L3
- Margon, B. 1984, *ARA&A*, 22, 507
- Margon, B., & Anderson, S. F. 1989, *ApJ*, 347, 448
- Marshall, F. E., Swank, J. H., Boldt, E. A., Holt, S. S. Serlemitsos, P. J. 1979, *ApJ*, 230, 145
- Porquet, D., & Dubau, J. 2000, *A&A*, 143, 495
- Vermeulen, R. C., Schilizzi, R. T., Spencer, R. E., Romney, J. D., and Fejes, I. 1993, *A&A*, 270, 177

Watson, M. G., Stewart, G. C., Brinkmann, W., and King, A. R. 1986, MNRAS, 222, 261

Watson, M. G., Willingale, R., Grindlay, J. E., and Seward, F. D. 1983, ApJ, 273, 688

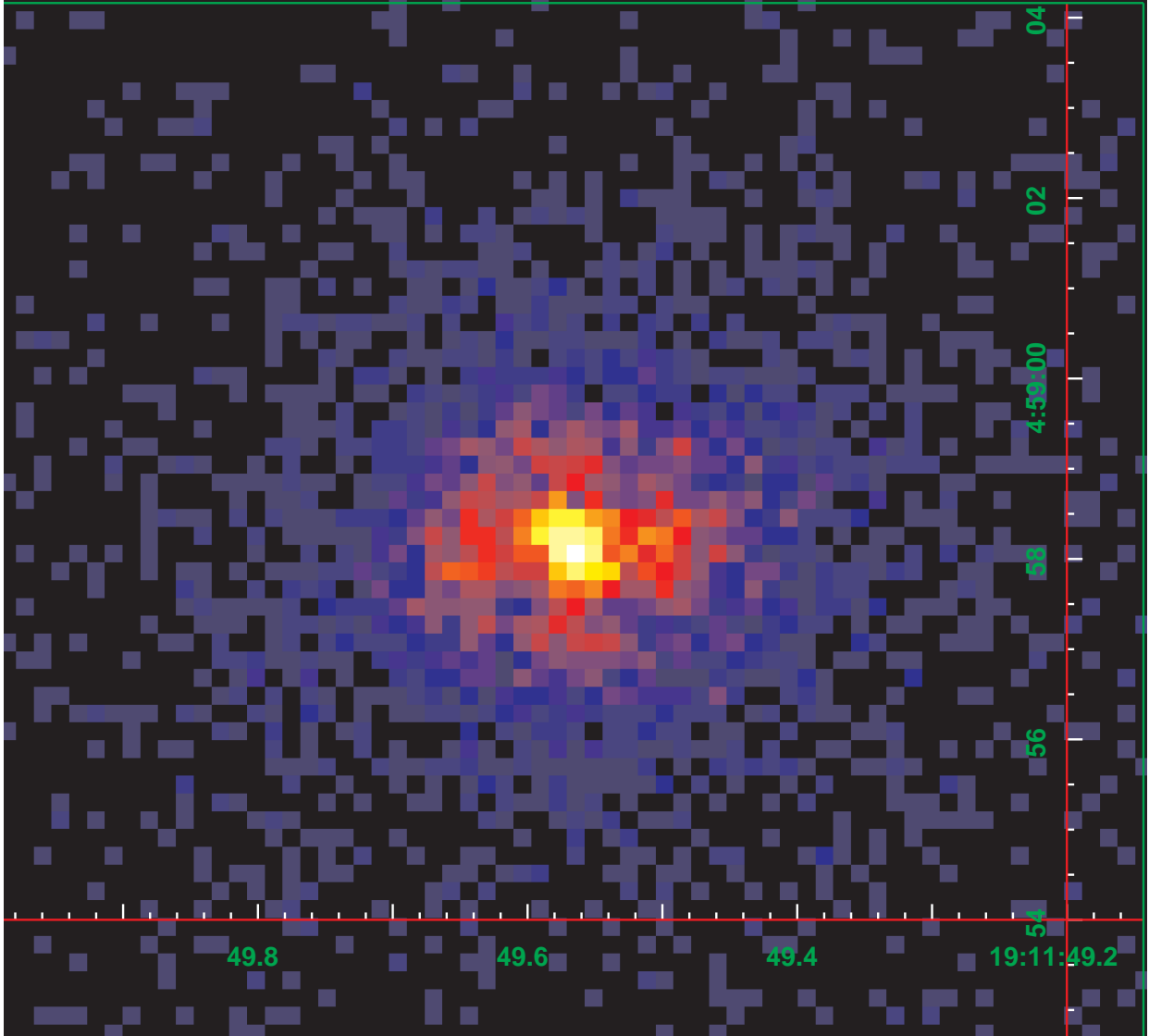


Fig. 1.— Image of SS 433 from the zeroth order of the *Chandra* High Energy Transmission Grating Spectrometer. The dispersion direction is approximately aligned with the north-south direction. The image is extended along the east-west direction on a scale of 2-5". The extent is comparable to that observed in the radio band (Hjellming & Johnston 1981).

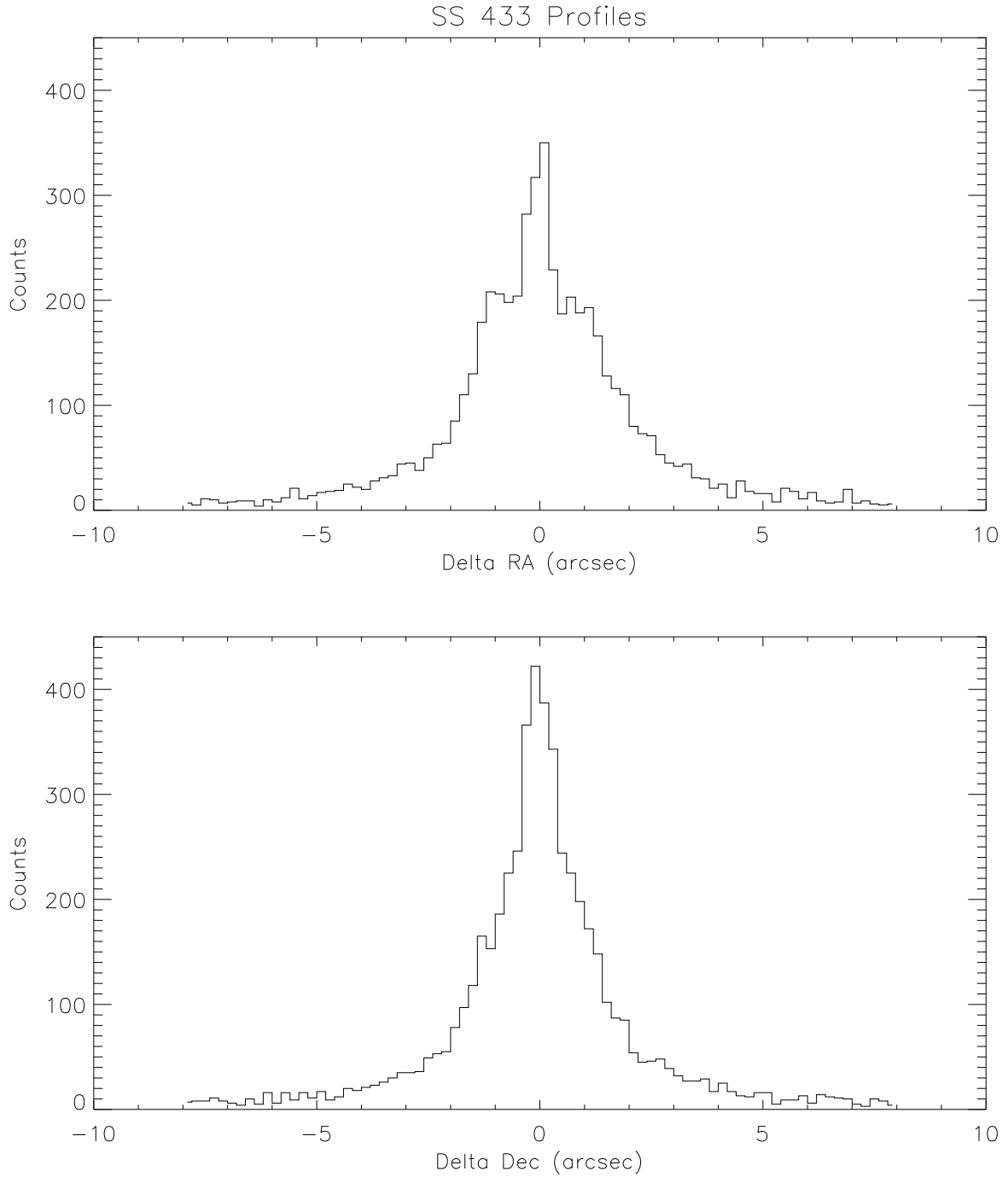


Fig. 2.— One dimensional profiles of the zeroth order image shown in figure 1. *Top:* East-west direction, which is nearly aligned with the radio jets observed by (Hjellming & Johnston 1981). *Bottom:* North-south direction. The difference between the N-S and E-W profiles is significant and is independent of the distortions of the point response that occurs due to event pileup (see text).

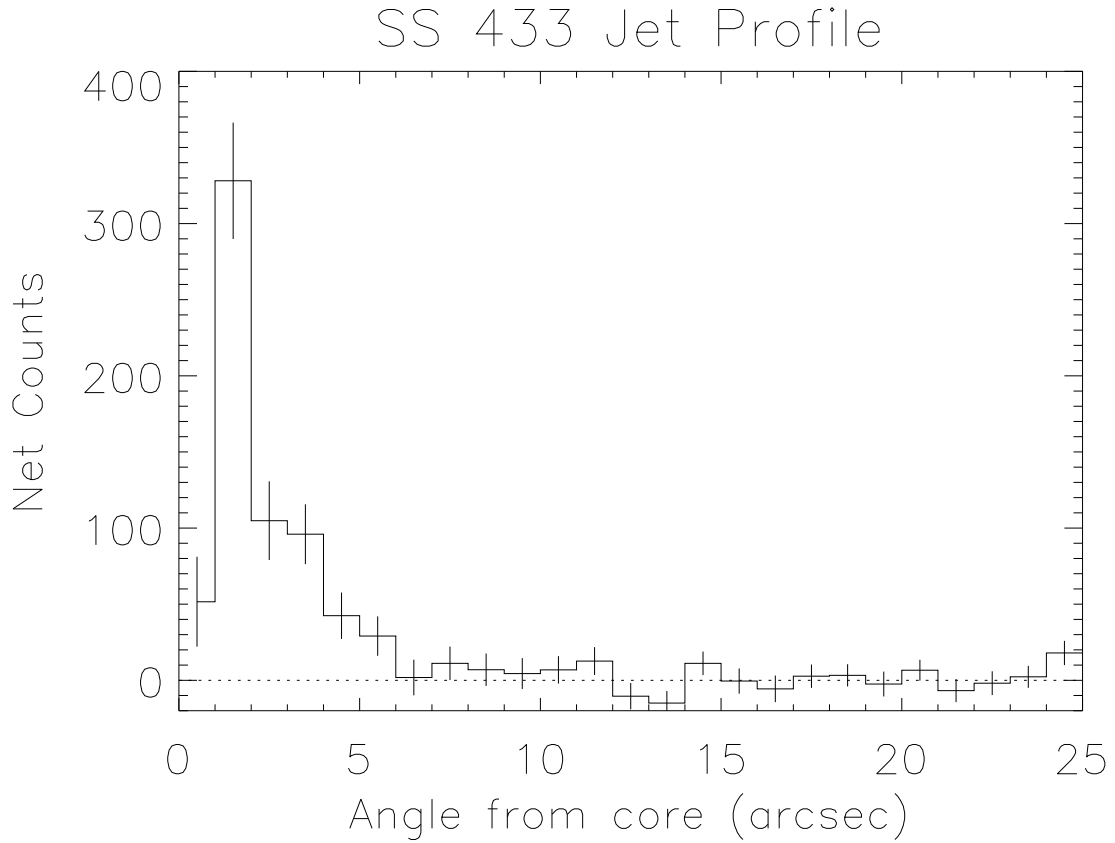


Fig. 3.— Profile of the  $2''$  scale X-ray jet. North and south sectors were used as background so that the core point source is eliminated from the east-west sectors and the flux in the first bin is nulled. The jets are brightest at about  $1.5''$  from the core and are no longer detectable beyond  $6''$ .

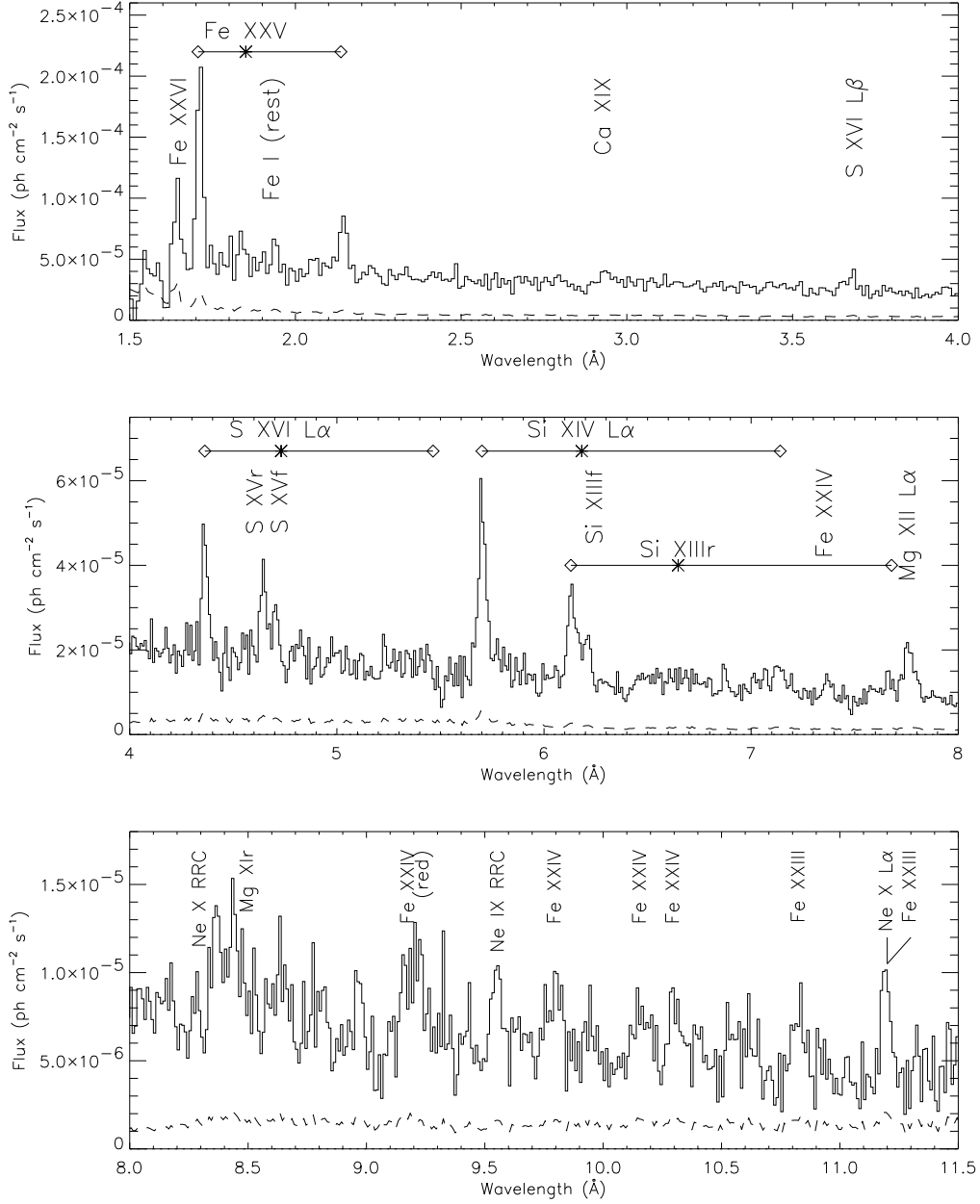


Fig. 4.— The X-ray spectrum of SS 433 observed with the Chandra High Energy Transmission Grating Spectrometer. The HEG and MEG data were combined at the resolution of the MEG spectrum. Line identifications are shown and measurements are given in table 1. All lines originate in the blue jet unless shown otherwise. Horizontal lines connect the locations of blue- and red-shifted lines (diamonds) to the rest wavelengths (asterisks). The dashed line gives the statistical uncertainties. Emission lines are resolved and their strengths indicate that the plasma is collisionally dominated. The Si XIII triplet is resolved in the HEG data, as shown in Fig. 8, and can be used to estimate the density of the emission region.

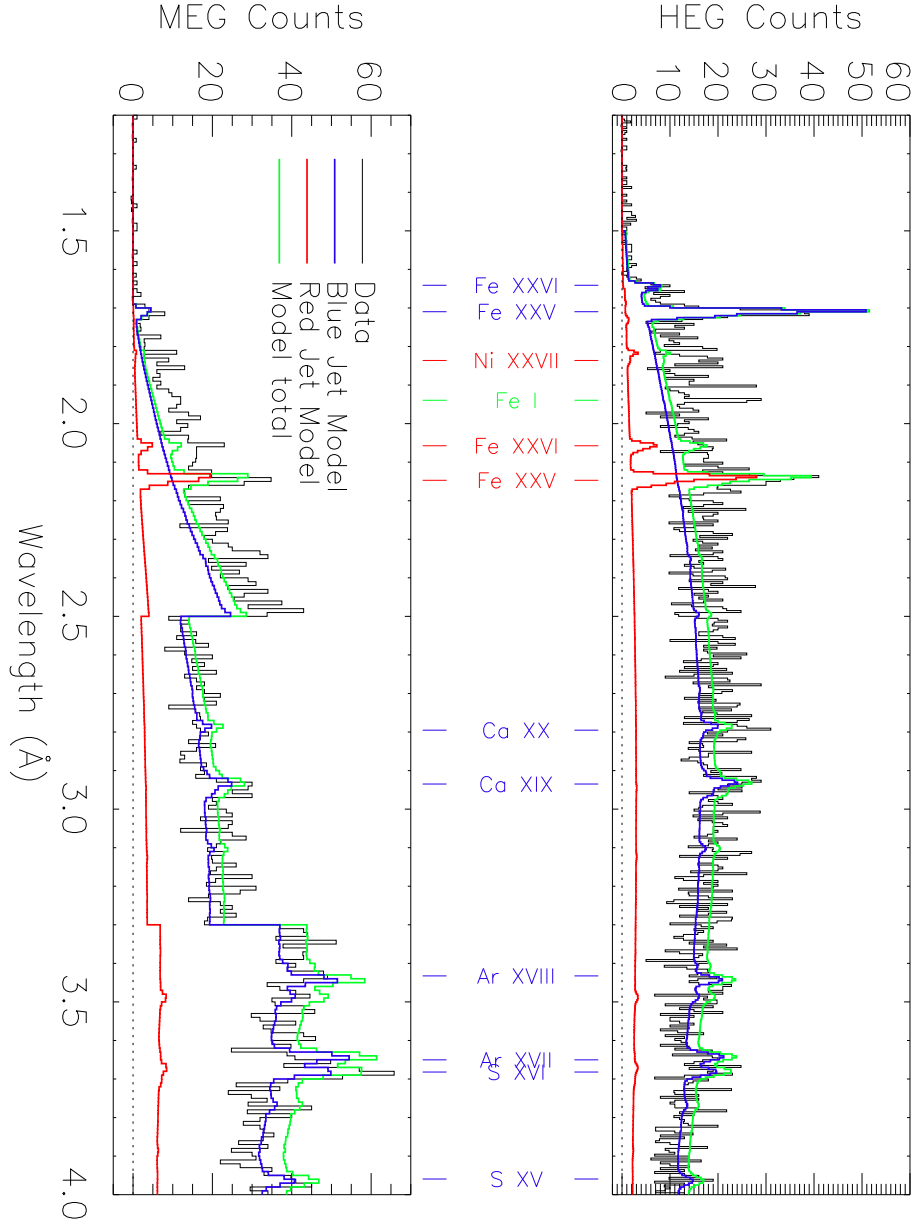


Fig. 5.— The 1.2-4.0 Å portions of the HEG and MEG spectra of SS 433 observed with the Chandra HETGS, compared to models of the spectra of the blue and red jets. The sum of the red and blue spectra give the green curve. Line identifications are shown and measurements are given in table 1. The continuum is dominated by thermal bremsstrahlung emission. Edges in the MEG spectrum at 2.5Å and 3.3Å are the result of excising data near the detector chip gaps (see text).

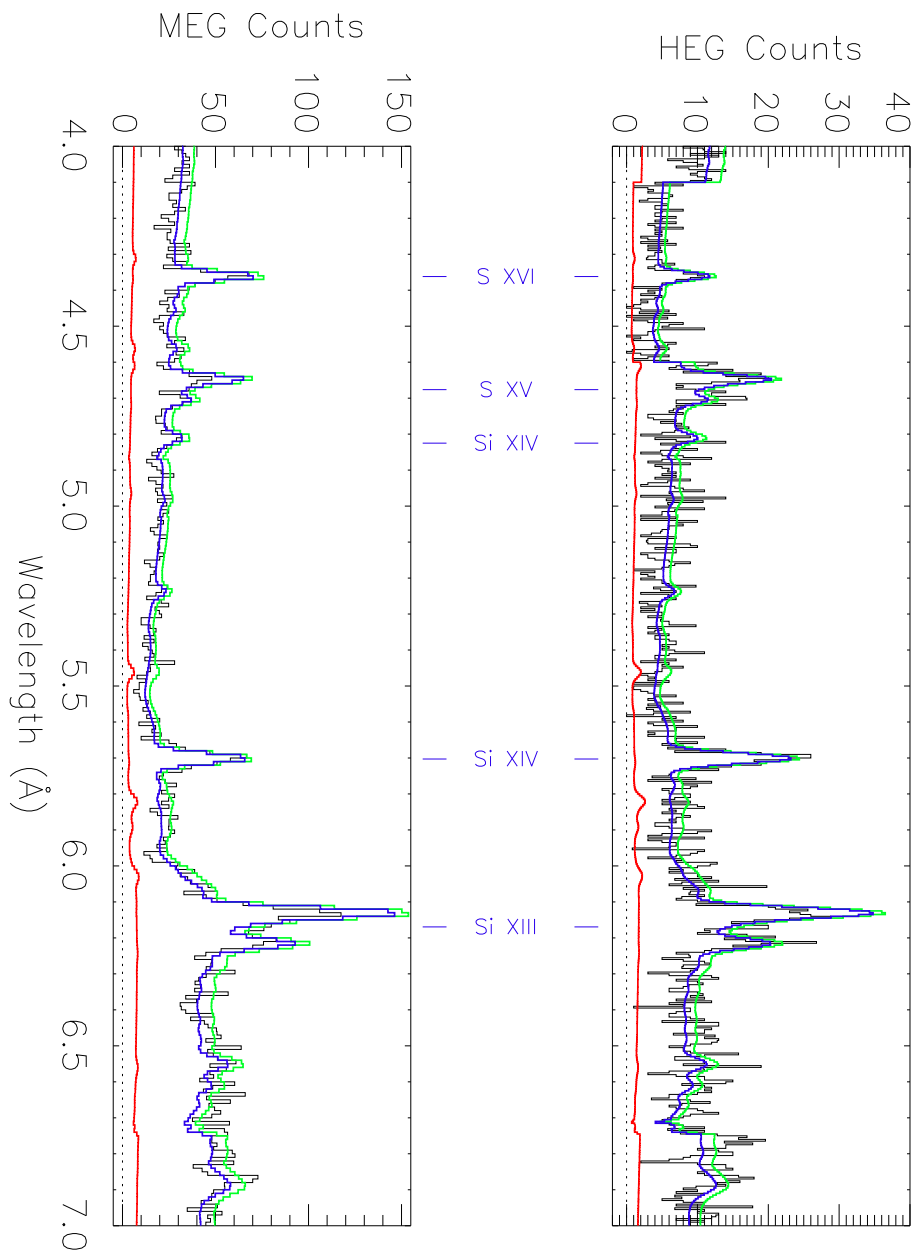


Fig. 6.— Same as figure 5 except for the 4-7Å region. Lines from the red jet are not very strong in this portion of the spectrum. The overall model continuum is slightly higher than the data in the 4-6Å range. Due to limitations of the modelling code, density-sensitive emission lines are not accurately represented. A better model of the Si XIV and Si XIII lines is shown in detail in Fig. 8.

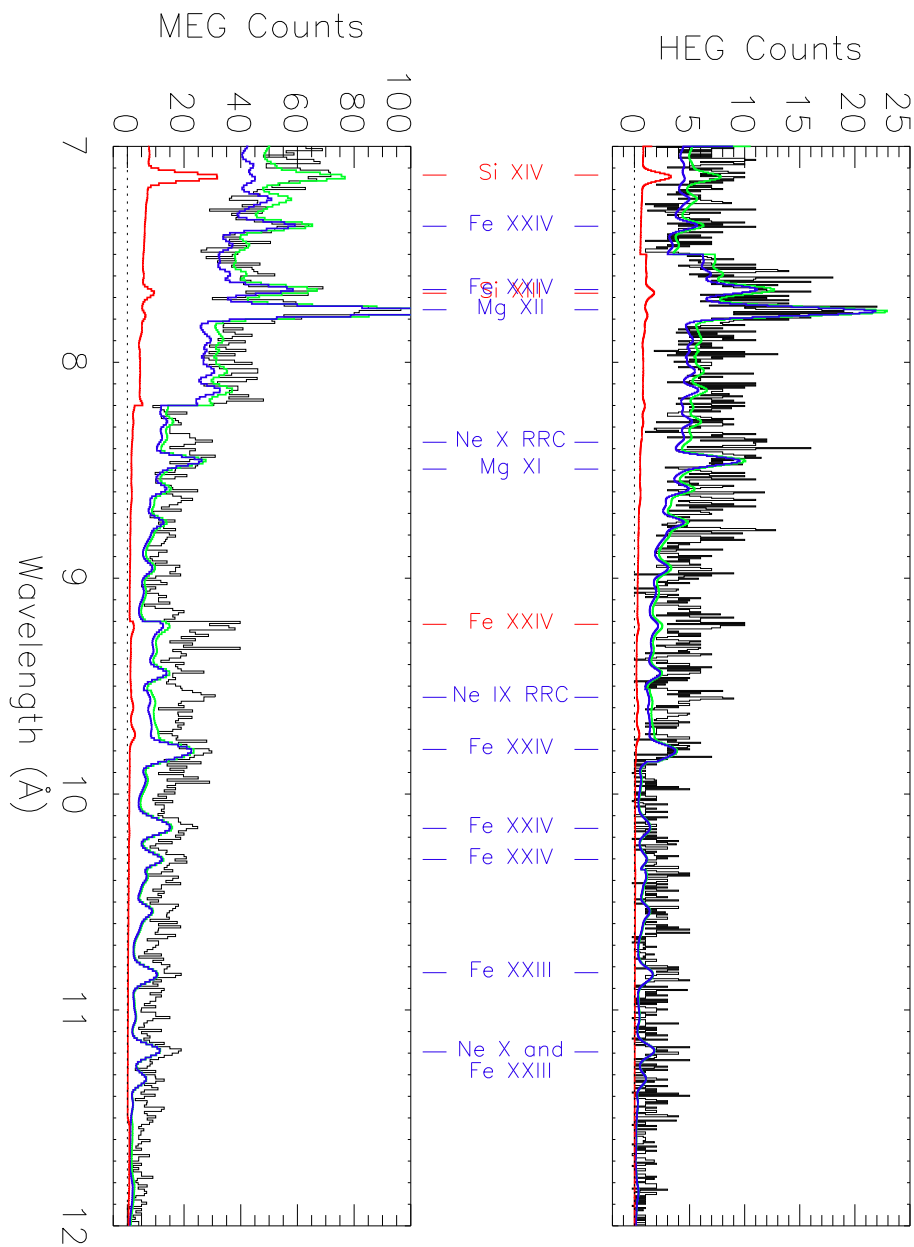


Fig. 7.— Same as figure 5 except for the 7-12Å region. The overall model continuum is slightly lower than the data in this wavelength range. Two blueshifted radiative recombination continuum (RRC) features are marked. The RRC features are not predicted by the model which assumes purely collisional ionization balance.

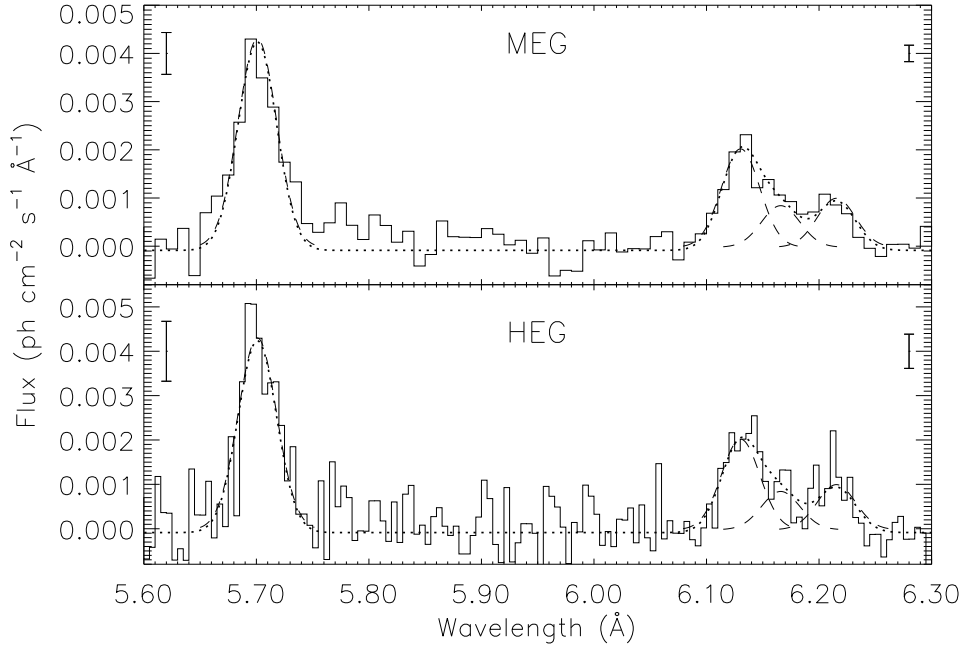


Fig. 8.— Detail of Gaussian modelling of the Si XIV and Si XIII lines. The dotted line gives the combined spectral model and the components are shown with dashed lines. Two typical error bars are shown in each panel. The Gaussian dispersions were constrained to be identical for all lines and the rest wavelengths of all lines were fixed so there were only six parameters in the model: Doppler shift, line width, two line strengths (Si XIV Ly $\alpha$  and Si XIII resonance), and the ratios  $G = (i + f)/r$  and  $R = f/i$ , where  $r$ ,  $i$ , and  $f$  are the strengths of the Si XIII resonance, intercombination, and forbidden lines, respectively. A simple continuum model was subtracted from the spectrum.

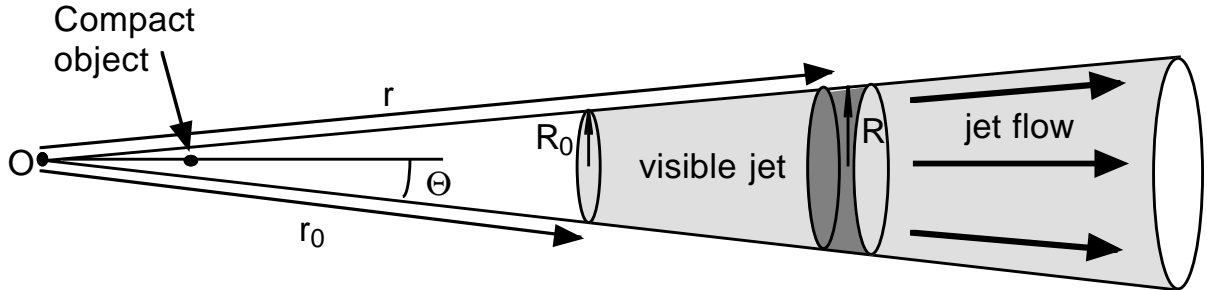


Fig. 9.— Geometry of a jet with uniform velocity outflow. The jet flow is radial, so quantities such as density and temperature can be given in terms of  $r$ , the distance from the cone's apex at  $O$ . The visible portion of the jet is shaded and its base is at a distance  $r_0$  from the apex. The compact object is on the jet axis at some distance less than  $r_0$  from  $O$ . The radius of the jet cross section is  $R = \Theta r$  and the radius at the base is  $R_0 = \Theta r_0$ .

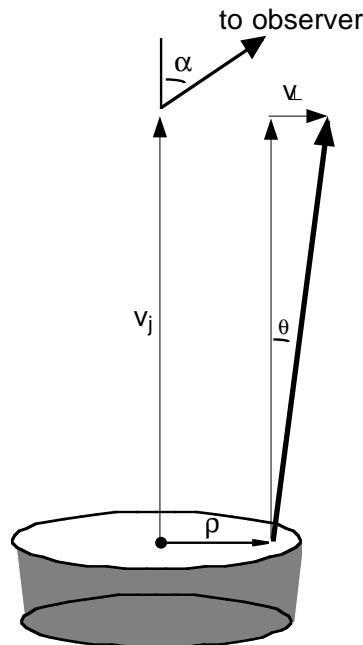


Fig. 10.— Geometry of a differential slice of the jet, indicating the various angles in the system. The jet axis is viewed at an angle  $\alpha$  to the line of sight and  $\theta$  is the flow direction of a jet fluid element relative to the jet axis. Gas with constant line-of-sight velocity,  $v$ , relative to the on-axis flow, lies along a chord at distance  $\rho = \theta r$  from the jet axis perpendicular to the direction to the observer.

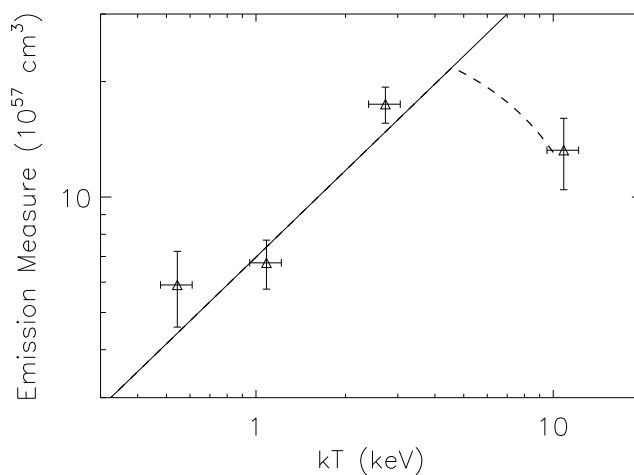


Fig. 11.— Emission measure *vs.* temperature from the multi-temperature fits to the blue jet line fluxes. The vertical error bars are determined from the fit while the horizontal error bars denote the coarseness of the temperature grid used. The line gives the relation expected for an adiabatically expanding uniform outflow in the asymptotic limit. The high  $T$  point is low by a factor of 2, which may result from increased optical thickness or perhaps truncation of the jet. The dashed line gives a model of the emission measure that accounts for the decreased volume of a jet that is truncated at  $r = 2.1 \times 10^{10}$  cm with a maximum temperature of  $1.1 \times 10^8$  K.

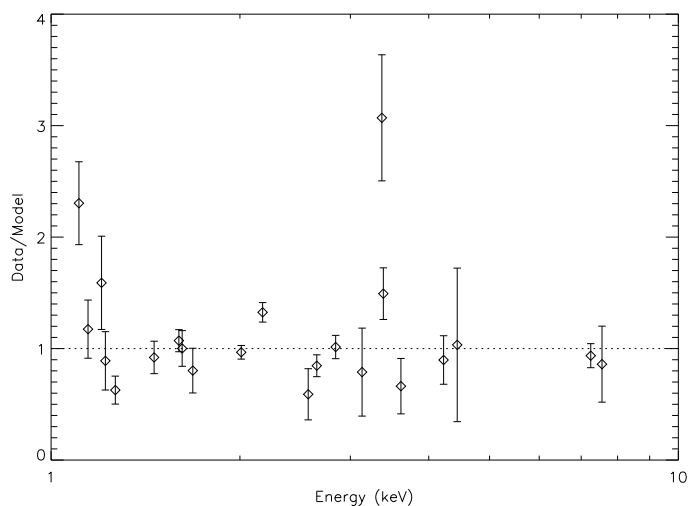


Fig. 12.— Ratio of the observed line flux to that predicted from the four component thermal model given in table 4. Most line fluxes agree with the model to within 50%.

Table 1. SS 433 X-ray Emission Lines

$\lambda_{rest}$ (Å)	$\lambda_{obs}$ (Å)	$z$	Flux ( $10^{-6}$ ph cm $^{-2}$ s $^{-1}$ )	Identification
Blue Jet				
1.780	1.641 ± 0.002	-0.0779 ± 0.0012	111 ± 44	Fe XXVI Ly $\alpha$ <sup>a</sup>
1.855	1.710 ± 0.001	-0.0781 ± 0.0005	373 ± 43	Fe XXV 1s2p-1s $^2$
3.020	2.795 ± 0.006	-0.0745 ± 0.0021	12 ± 8	Ca XX Ly $\alpha$
3.186	2.935 ± 0.004	-0.0788 ± 0.0013	34 ± 8	Ca XIX 1s2p-1s $^2$
3.733	3.432 ± 0.006	-0.0805 ± 0.0015	16 ± 6	Ar XVIII Ly $\alpha$
3.952	3.650 ± 0.003	-0.0764 ± 0.0009	20 ± 6	Ar XVII 1s2p-1s $^2$
3.991	3.682 ± 0.002	-0.0774 ± 0.0005	38 ± 7	S XVI Ly $\beta$
4.299	3.959 ± 0.006	-0.0791 ± 0.0013	12 ± 6	S XV 1s3p-1s $^2$
4.729	4.362 ± 0.002	-0.0776 ± 0.0003	97 ± 10	S XVI Ly $\alpha$
5.055	4.675 ± 0.004	-0.0778 ± 0.0003	121 ± 14	S XV 1s2p-1s $^2$ <sup>d</sup>
5.217	4.825 ± 0.005	-0.0752 ± 0.0010	18 ± 7	Si XIV Ly $\beta$
6.182	5.703 ± 0.002	-0.0776 ± 0.0002	182 ± 12	Si XIV Ly $\alpha$
6.675	6.169 ± 0.003	-0.0779 ± 0.0002	158 ± 10	Si XIII 1s2p-1s $^2$ <sup>d</sup>
7.986	7.370 ± 0.005	-0.0771 ± 0.0006	16 ± 4	Fe XXIV
8.310	7.663 ± 0.004	-0.0779 ± 0.0005	25 ± 4	Fe XXIII/XXIV
8.421	7.756 ± 0.002	-0.0789 ± 0.0003	54 ± 5	Mg XII Ly $\alpha$ <sup>b</sup>
9.102	8.370 ± 0.004	-0.0803 ± 0.0004	26 ± 5	Ne X RRC <sup>c</sup>
9.181	8.495 ± 0.018	-0.0747 ± 0.0020	38 ± 6	Mg XI 1s2p-1s $^2$
10.368	9.552 ± 0.005	-0.0788 ± 0.0004	24 ± 4	Ne IX RRC <sup>c</sup>
10.634	9.795 ± 0.006	-0.0789 ± 0.0005	20 ± 4	Fe XXIV <sup>e</sup>
11.008	10.159 ± 0.010	-0.0771 ± 0.0009	17 ± 5	Fe XXIV <sup>e</sup>
11.176	10.303 ± 0.007	-0.0781 ± 0.0006	19 ± 5	Fe XXIV
11.736	10.827 ± 0.007	-0.0775 ± 0.0006	18 ± 4	Fe XXIII
12.134	11.194 ± 0.004	-0.0783 ± 0.0003	31 ± 5	Ne X Ly $\alpha$ & Fe XXIII
Rest frame				
1.937	1.939 ± 0.002	0.0010 ± 0.0008	49 ± 14	Fe I
Red Jet				
1.592	1.836 ± 0.003	0.1538 ± 0.0016	55 ± 16	Ni XXVII 1s2p-1s $^2$
1.780	2.057 ± 0.005	0.1560 ± 0.0026	22 ± 10	Fe XXVI Ly $\alpha$
1.855	2.147 ± 0.001	0.1577 ± 0.0006	129 ± 16	Fe XXV 1s2p-1s $^2$
6.182	7.133 ± 0.004	0.1537 ± 0.0006	34 ± 4	Si XIV Ly $\alpha$
6.675	7.747 ± 0.018	0.1610 ± 0.0026	25 ± 4	Si XIII 1s2p-1s $^2$ <sup>b</sup>
7.986	9.214 ± 0.006	0.1538 ± 0.0007	27 ± 4	Fe XXIV

<sup>a</sup>Only HEG data were used.

<sup>b</sup>Mg XII from the blue jet is somewhat confused with Si XIII from the red jet. There is also an Fe XXIV line from the blue jet near the location of the Si XIII resonance line.

<sup>c</sup>Radiative recombination continua.

<sup>d</sup>He-like triplet system fitted with three lines with independent fluxes and fixed rest wavelengths.

<sup>e</sup>Blend; rest wavelength is based on a flux-weighted average.

Table 2. Line Widths

Wavelength Range (Å)	$v^a$ (km s <sup>-1</sup> )
1.5 – 2.5	892 ± 162
2.5 – 4.0	741 ± 138
4.0 – 5.5	742 ± 75
5.5 – 7.5	810 ± 61
7.5 – 10.0	656 ± 75
10.0 – 11.5	595 ± 86

<sup>a</sup>Velocity width ( $\sigma$ ) of Gaussian line profiles.

Table 3. Estimated Temperatures and Emission Measures from Line Ratios using Single Temperature Models

Element	Blue Jet		Red Jet	
	$T$ (10 <sup>6</sup> K)	$EM_{1T}^a$ (10 <sup>57</sup> cm <sup>3</sup> )	$T$ (10 <sup>6</sup> K)	$EM_{1T}^a$ (10 <sup>57</sup> cm <sup>3</sup> )
Fe	88	20.1	71	3.9
Ca	41	26.1	...	...
Ar	23	27.0	...	...
S	26	21.0	...	...
Si	19	18.5	20	2.4
Mg	13	8.0	...	...

<sup>a</sup>Emission measure for a single temperature model that reproduces that elements’ H- and He-like emission line fluxes at a distance of 4.85 kpc, for an interstellar absorption column density of 10<sup>22</sup> cm<sup>-2</sup>, and corrected for Doppler shifts.

Table 4. Blue Jet Parameters from a Multi-Temperature Model<sup>a</sup>

$T$ ( $10^6$ K)	$EM$ ( $10^{57}$ cm <sup>3</sup> )	$r$ ( $10^{10}$ cm)	$n_e$ ( $10^{14}$ cm <sup>-3</sup> )
6.3	$5.90 \pm 1.32$	20.5	0.45
12.6	$6.57 \pm 1.00$	12.2	1.00
31.6	$18. \pm 1.92$	6.13	4.66
126.	$12.8 \pm 2.87$	2.17	18.6

<sup>a</sup>The interstellar absorption column density was fit simultaneously with the  $EM$  values at each temperature. The best fit absorption column was  $2.20 \pm 0.07 \times 10^{22}$  cm<sup>-2</sup>. The temperatures were set to values on a logarithmic grid which minimized the  $\chi^2$ .